# Three-dimensional acoustic propagation model for shallow waters based on an indirect boundary element method

Edmundo F. Lavia[1,2,†], Juan D. Gonzalez[1,2], and Silvia Blanc[1,2]

[1] *Acoustic Propagation Department, Argentinian Navy Research Office (DIIV), Buenos Aires* 1638, *Argentina*
[2] *UNIDEF (National Council of Scientific and Technical Research/Ministry of Defense), Buenos Aires, Argentina*

(Received 28 May 2022; revised manuscript received 14 August 2022; accepted manuscript online 9 September 2022)

This work has a two-fold purpose. On the one hand, the theoretical formulation of a three-dimensional (3D) acoustic propagation model for shallow waters with a constant sound speed is presented, based on the boundary element method (BEM), which uses a half-space Green function instead of the more conventional free-space Green function. On the other hand, a numerical implementation is illustrated to explore the formulation in simple idealized cases, controlled by a few parameters, which provides necessary tests for the accuracy and performance of the model. The half-space Green's function, which has been previously used in scattering and diffraction, adds terms to the usual expressions of the integral operators without altering their continuity properties. Verifications against the wavenumber integration solution of the Pekeris waveguide suggest that the model allows an adequate prediction for the acoustic field. Likewise, numerical experiments in relation to the necessary mesh size for the description of the water-marine sediment interface lead to the conclusion that a transmission loss prediction with acceptable accuracy can be obtained with the use of a limited mesh around the desired evaluation region.

**Keywords:** three-dimensional acoustic propagation, boundary element method, half-space Green function

**PACS:** 43.20.Rz, 43.30.+m, 92.10.Vz **DOI:** 10.1088/1674-1056/ac90b1

## 1. Introduction

Underwater sound propagation is significantly affected by three-dimensional (3D) effects due to the complex realistic ocean environment. The importance of these effects has been early recognised[1,2] and even emphasized by at-sea and/or at-laboratory measurements.[3]

A great variety of models have been developed to estimate underwater sound propagation in 3D scenarios which, according to their governing equations and numerical approaches, can be categorized into three main groups,[4] namely, (a) extended parabolic equation (PE) models, such as the efficient marching solution based on the parabolic equation[5] that has been applied to a local and a global ocean environment;[6,7] (b) normal mode models;[8–11] and (c) ray and beam tracing models.[12,13] However, modelling acoustic propagation for 3D environments is still a significant two-fold challenge due to both the difficulties associated with a thorough comprehension of the physical phenomenon and the high computational time costs.

The continuous growth in computational power (hardware equipped with more raw processing power and more memory capacity) opens up the game for methods based on volume or boundary discretization as the finite element method (FEM) and the boundary element method (BEM) (these examples are not exhaustive, see Ref. [14] for a wide review about underwater acoustic models under the high performance computer paradigm). These methods allow for a more realistic modelling since they assume fewer hypotheses than classical and well established ones as the ray methods, PE methods and coupled normal modes,[15] which have been successfully used for several decades. The above mentioned restrictive assumptions generally refer to symmetry conditions and/or their validity limited to certain frequency regimes.

The BEM consists in defining the acoustic field through surface-integral operators which reduce the definition of the computational domain from 3D to 2D. Regarding underwater sound propagation, several references can be found in the literature such as a previous work that used a multi-layer approach for shallow waters by defining boundary integral equations whose unknowns are the pressure field and the normal particle velocity on the surfaces.[16] This approach is categorized as a direct BEM. Although the BEM is computationally more expensive than other methods, acceleration algorithms can be used to improve its performance. It is still not capable to model realistic scenarios for long-range propagation such as those involved in some applications where the propagation range has several thousand of kilometres.[17,18] Nevertheless, the method still has its strong advantages such as a clean mathematical formulation and a consistent behaviour at infinity (where the fields are expected to vanish).

In this work, we present a numerical implementation of an indirect BEM capable of tackling the acoustic propagation problem in a homogeneous medium with an arbitrary bathymetry (range-dependent model) that can be easily ex-

[†]Corresponding author. E-mail: sivasadartantasvueltasnosirve@gmail.com

© 2023 Chinese Physical Society and IOP Publishing Ltd 

tended to a multilayer coupled approach to consider inhomogeneous media. This formulation includes an appropriate half-space Green function to take into account an infinite pressure release surface, which is a representation of the ocean free surface in an exact analytical way. Accordingly, generation of a mesh corresponding to the interface ocean-atmosphere is avoided. This idea has already been used for a boundary integral equation method (BIEM) solution for the acoustic scattering from the surface of a waveguide then applied to a 2D case with non-penetrable boundaries,[19] for a 2D waveguide with a more general Green function[20,21] and within the context of acoustic scattering and radiation.[22] Furthermore, from the computational point of view, the indirect approach leads to operators that are numerically well-behaved in comparison with the direct methods needing some preconditioners in order to solve the problem.[16]

This paper is organized as follows. In Section 2, the BEM model is presented. The boundary value problem corresponding to acoustic propagation in a waveguide is stated in Subsection 2.1, then the BEM theoretical formulation based on a half-space Green function – emphasizing the differences with those based on the free-space function – is developed in Subsection 2.2 and finally an outline of the numerical method is provided in Subsection 2.3. Certain more technical mathematical aspects and some intermediate steps in the derivations are confined to the appendices. In Section 3, numerical experiments aided to verify the BEM model are carried out. To this end a wave-number integration technique applied to the propagation problem of a Pekeris waveguide provided with a sediment layer (with and without attenuation) is used as a benchmark. Section 4 shows the performance of the model in a shallow water waveguide with a conical mountain, which provides a range-dependent bathymetry. The conclusions of the work and suitable further steps aimed to improve the model are summarized in Section 5.

## 2. Model formulation

### 2.1. Acoustic propagation problem

The problem of the underwater sound propagation in a homogeneous waveguide with range dependent bathymetry is schematically shown in Fig. 1. A time harmonic point source of circular frequency $\omega$ is located in a homogeneous water layer (which defines the volumetric region $R_0$) bounded above by the plane surface $\Gamma_0$ and below by the arbitrary surface $\Gamma_1$. The latter limits an unbounded volumetric region $R_1$ that constitutes a marine sediment layer. The surfaces $\Gamma_0$ and $\Gamma_1$ represent the interfaces seawater-atmosphere and seawater-marine sediments, respectively. Each region $R_i$ $(i = 0, 1)$ is characterized by constant acoustic properties $c_i$ and $\rho_i$ (sound speed and density) and wavenumber $k_i = \omega/c_i$. The boundless nature of the $R_1$ region is emphasized in the scheme by the dashed line at the bottom.

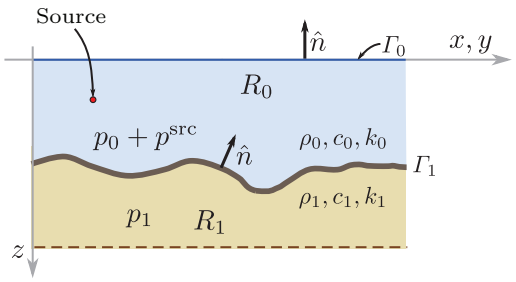



**Fig. 1.** Scheme for the propagation problem. It should be noted that neither cylindrical nor plane symmetry must be inferred from this 2D sketch.

The given point source generates, through interaction with the boundaries, acoustic pressure fields $p_i$ in each region $R_i$ that are solutions of the scalar Helmholtz equation

$$(\nabla^2 + k_i^2)p_i = 0, \quad i = 0, 1. \tag{1}$$

If the source field is $p_i$, then the total field in the region $R_0$ is $p = p_0 + p_i$. As it is usual in propagation problems, the boundary condition at $\Gamma_0$ assumes a pressure-release surface (Dirichlet condition: $p_0 + p_i = 0$), whereas at $\Gamma_1$ the pressure field must satisfy the transmission condition that arises from demanding continuity of both the field and the normal particle velocity $v_n = -1/(\mathrm{i}\omega\rho)\partial_n p$ (the notation $\partial_n$ is a common abbreviation for the normal derivative $\hat{n}\cdot\nabla$). The point source located at $x_{\mathrm{src}}$ is assumed to generate a field

$$p_i(x) = \frac{\mathrm{e}^{\mathrm{i}k_0|x-x_{\mathrm{src}}|}}{|x-x_{\mathrm{src}}|},$$

with unitary amplitude.

According to the mathematical framework appropriate to BEM (integral operators theory), it is convenient[23] to transform the fields according to

$$u_0 = \frac{p_0}{\rho_0}, \quad u_1 = \frac{p_1}{\rho_1}, \quad u^{\mathrm{src}} = \frac{p_i}{\rho_0}, \tag{2}$$

which has the consequence of making the factors $\rho_i^{-1}$ drop out from the normal derivatives. In terms of these fields $u_i$, the pressure release condition at $\Gamma_0$ leads to

$$u_0(x) + u^{\mathrm{src}}(x) = 0 \quad \text{for} \quad x \in \Gamma_0, \tag{3}$$

whereas the requirement of continuity in the field and its derivative at $\Gamma_1$ (i.e., the boundary conditions at the interface) implies

$$\left.\begin{aligned} \rho_0 u_0(x) - \rho_1 u_1(x) &= -\rho_0 u^{\mathrm{src}}(x) \\ \partial_n u_1(x) - \partial_n u_1(x) &= -\partial_n u^{\mathrm{src}}(x) \end{aligned}\right\} \text{for } x \in \Gamma_1. \tag{4}$$

The differential equations given in Eq. (1) and the conditions of Eqs. (3) and (4) constitute the boundary value problem that models the acoustic propagation problem schematized in Fig. 1. In the next section, this problem will be posed under a mathematical formulation appropriate for an indirect BEM approach.

### 2.2. BEM formulation with a half-space Green function

A typical indirect BEM formulation for the acoustic propagation problem previously introduced presupposes that each field $u_i$ is expressed as a linear combination of certain kind of surface integrals as, for example, in

$$u_i(x) = a\int_\Gamma \Phi(x,y)\varphi(y)\,\mathrm{d}S_y + b\int_\Gamma \partial_{n_y}\Phi(x,y)\sigma(y)\,\mathrm{d}S_y, \quad (5)$$

where the kernel function $\Phi(x,y)$ and its normal derivative are two-point functions, which give the field $x$-dependence, while the integration (over the boundary $\Gamma$) is carried out in the $y$-variable, and the latter is emphasized by the sub-index in the surface differential $\mathrm{d}S_y$. Coefficients $a$ and $b$ are known constants while $\varphi$ and $\sigma$ are functions to be determined. Each integral in Eq. (5) can be interpreted as an integral operator[24] acting on a function, for which the usual nomenclature is

$$U[\varphi](x) = \int_\Gamma \Phi(x,y)\varphi(y)\,\mathrm{d}S_y, \quad (6)$$

where $U$ represents the operator (associated with a kernel $\Phi$), and $\varphi$ the function integrated on the surface $\Gamma$. As will be seen later, the field-values $\varphi(y)$ on $\Gamma$ will be unknown quantities for the integral formulation of our boundary value problem for acoustic propagation.

In the vast majority of 3D BEM applications associated to the Helmholtz equation, the kernel function $\Phi(x,y)$ is the free-space Green function in the wavenumber $k_i$,

$$G(k_i;x,y) = \frac{\mathrm{e}^{\mathrm{i}k_i|x-y|}}{4\pi|x-y|}, \quad (7)$$

which has the property of being a solution of the Helmholtz equation in absence of boundaries (that is the reason why it is dubbed free-space). It should be noted that if the kernel satisfies the Helmholtz equation (where the Laplacian is taken with regard to the $x$-variable) then its associated operator also does it, as long as the interchange between the integral sign and the Laplacian is possible. This kernel $G(k_i;x,y)$ and its normal derivative define the operators

$$S_i[\varphi](x) = \int_\Gamma G(k_i;x,y)\varphi(y)\,\mathrm{d}S_y,$$
$$K_i[\varphi](x) = \int_\Gamma \partial_{n_y}G(k_i;x,y)\varphi(y)\,\mathrm{d}S_y,$$

in which the sub-index associates the operator with the wavenumber $k_i$ or equivalently with the $R_i$ region. These operators $S_i$ and $K_i$ constitute the basis for all BEM methods and are called the single layer potential operator (SLP) and the double layer potential operator (DLP), respectively. Since the spherical symmetry of $G(k_i;x,y)$ offers no special advantages for the propagation problem under consideration (because the boundaries are not spherical), a typical BEM formulation would involve integration in both $\Gamma_0$ and $\Gamma_1$, i.e., it would require numerical discretization of both of these boundaries.

It is also worth noting that although the water and sediment layers are schematized in Fig. 1 without borderlines in the $x$, $y$ directions in the underwater acoustic propagation modelling, it is assumed that these limits are far away from the area of interest so their effects can be neglected. In fact, this assumption implies that the solution for a limited area near the source is identical to a solution for an acoustic problem, which has those limits located at infinity. By using this feature it is possible to use a modified Green function, which takes into account part of the boundaries of the problem in an exact way, avoiding thus the need of building a discretized version of those boundaries and consequently also avoiding integrating over them.

Beyond the free-space Green function, the simplest useful modification is the half-space Green function, obtained by using the image method,[25] which is of widespread application in acoustics and optics (the Rayleigh–Sommerfeld correction to the problem of diffraction by an aperture being an iconic example). The half-space Green function appropriate to our problem will be the solution of the Helmholtz equation valid for a semi-space $z > 0$, where the (infinite) boundary plane $z = 0$ is such that over it the Green's function becomes zero. Its expression is

$$\bar{G}(k_i,x,y) = G(k_i;x,y) - \frac{\mathrm{e}^{\mathrm{i}k_i|x-y'|}}{4\pi|x-y'|}, \quad (8)$$

where $y'$ is the specular image of the point $y$ by the plane $z = 0$. Figure 2 shows the points $x, y, y'$ involved in the definition of $\bar{G}$. It is important to emphasize that the modification in Eq. (8) (an extra term) can be interpreted as a new source, an image source located at point $y'$ outside of the physical region, where the acoustic problem is being solved. The idea of extending the physical domain by adding extra-termns has already been used in the context of the parabolic wave approximation for shallow waters in 2D modelling. In Ref. [26], the authors used it to satisfy a pressure release condition in a flat ocean surface ($z = 0$), and in Refs. [27,28] that was generalized to treat rough surfaces of the form $z = \eta(r)$.

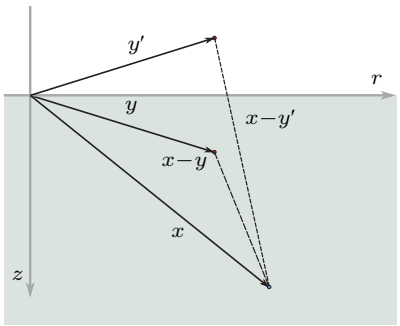



**Fig. 2.** Points and vectors associated to the half-space Green function. For point $x, y$ appearing in the argument of the usual Green function, the half-space variant considers a point $y'$, specular reflection of $y$ by the $z = 0$ plane.

Regarding the propagation problem depicted in Fig. 1, the use of a half-space Green function as kernel in the $S$, $K$ operators implies that the propagation problem has a pressure-release surface condition built-in, in the sense that $u_0$ according to (5) verifies $u_0 = 0$ over $\Gamma_0$. However, as it is stated in the condition (3), it is desirable a little more on $\Gamma_0$, namely, $u_0 + u^{\text{src}} = 0$, which can be attained by redefining $u_0$ as $u_0 - u^{\text{src}\prime}$, where $u^{\text{src}\prime}$ is the image source

$$u^{\text{src}\prime}(x) = \frac{1}{\rho_0} \frac{\mathrm{e}^{\mathrm{i}k_0|x-x_{\text{src}}{}'|}}{|x-x_{\text{src}}{}'|}.$$

The problem solution in terms of these operators, plus the subtraction of the image source, automatically will take into account the surface $\Gamma_0$ so that an explicit evaluation of the boundary conditions is not necessary. The fields $u_i$ have now to fulfill boundary conditions only at $\Gamma_1$.

Furthermore, writing the solution through the half-space Green function implies that the solution of the propagation problem without the existence of $\Gamma_1$ (or with $\Gamma_1$ located at infinity) is (or tends to) the image solution

$$\bar{u}^{\text{src}} = u^{\text{src}} - u^{\text{src}\prime}, \tag{9}$$

which recovers the well known solution of the Lloyd's mirror problem.[25]

### 2.2.1. BEM formulation

Now, after having chosen an appropriate kernel function, the fields $u$ in each region $R$ will have the following integral representation:

$$u_0(x) = S_0[\phi](x) + K_0[\psi](x) - u^{\text{src}\prime}(x), \quad \text{for} \quad x \in R_0,$$

$$u_1(x) = S_1[\phi](x) + K_1[\psi](x) \quad \text{for} \quad x \in R_1, \tag{10}$$

where

$$S_i[\phi](x) = \int_{\Gamma_1} \bar{G}(k_i;x,y)\phi(y)\,\mathrm{d}S_y,$$
$$K_i[\psi](x) = \int_{\Gamma_1} \partial_{n_y}\bar{G}(k_i;x,y)\psi(y)\,\mathrm{d}S_y$$

are the SLP and the DLP operators, evaluated on the unknown functions $\phi$ and $\psi$, respectively. Since the boundary conditions of Eq. (4) involves the normal velocity, it will be necessary to evaluate normal derivatives of these operators. This procedure leads to two new operators

$$K_i'[\phi](x) = \partial_{n_x}\left(\int_{\Gamma_1} \bar{G}(k_i;x,y)\phi(y)\,\mathrm{d}S_y\right),$$
$$T_i[\psi](x) = \partial_{n_x}\left(\int_{\Gamma_1} \partial_{n_y}\bar{G}(k_i;x,y)\psi(y)\,\mathrm{d}S_y\right),$$

generically known as the normal derivative operators.[29]

The next step in the integral formulation is to evaluate the transmission conditions at $\Gamma_1$, Eq. (4), by using the field prescription according to (10). This process requires to carefully consider the operator's jump conditions (Subsection 3.1 of Ref. [24]) or, in other words, its behavior in the limit when its evaluation point $x$ in the surface is approached from $R_i$ along the normal vector direction $n_x$. Following these steps, the following system of two boundary integral equations:

$$\left.\begin{aligned}(\rho_0 K_0 - \rho_1 K_1 + 1/2\alpha_{01})[\psi](x) + (\rho_0 S_0 - \rho_1 S_1)[\phi](x) &= -\bar{u}^{\text{src}}(x)\\ -M_{01}[\psi](x) + (I - \rho_0 K_0' + \rho_1 K_1')[\phi](x) &= \partial_n \bar{u}^{\text{src}}(x)\end{aligned}\right\} \quad \text{for } x \in \Gamma_1 \tag{11}$$

for the two unknowns $\phi$ and $\psi$ is obtained, where $\alpha_{01} = (\rho_0 + \rho_1)/2$ and $M$ is another operator, called the Müller operator and defined as

$$M_{s\ell}[\varphi](x) \equiv T_s[\varphi](x) - T_\ell[\varphi](x). \tag{12}$$

Appendix A provides a schematic derivation of the system of Eq. (11) by evaluating carefully the limits and using the jump conditions from Ref. [24].

The modification in $\bar{G}$ with respect to the usual $G$, i.e., the addition of an image source at $y'$, modifies the usual expression for the integrands in the operators $S, K, K', T$. Nevertheless, these modifications does not alter its continuity and jump properties because the added term in $\bar{G}$ is regular for all $x, y$ in the physical domain. In Appendix B, expressions for all the four integral operator's kernels are provided.

The solution of the acoustic propagation problem given in terms of the fields $u_i$ has been transformed in the finding of the functions $\psi$ and $\phi$ both having the surface $\Gamma_1$ as their domains of definition. These functions are called densities in the literature and are now the unknowns. The BEM method provides a procedure to find discretized versions of these densities, which will be the subject of the next section.

## 2.3. Numerical method

The system of Eq. (11) can be solved through a discretization process over the boundary $\Gamma_1$, which turns it in a finite-size matrix system. For this step the standard procedure is to assume the following two approximations.

1. The surface $\Gamma_1$ is approximated by a planar triangular mesh (i.e., a set of $N_1$ triangles $\{\Delta_\ell\}$ with $\ell = 1, 2, \ldots, N_1$), so that

$$\Gamma_1 = \bigcup_{\ell=1}^{N_1} \Delta_\ell,$$

where $\Delta_\ell$ is the $\ell$-th triangle whose centroid is $x_\ell$.

2. The unknown densities $\psi$ and $\phi$ are considered as piecewise constant functions in each triangle, that is,

$$\psi(x) = \sum_{\ell=1}^{N_1} \psi_\ell I_{\Delta_\ell}(x), \quad \phi(x) = \sum_{\ell=1}^{N_1} \phi_\ell I_{\Delta_\ell}(x), \tag{13}$$

where $\psi_\ell$ and $\phi_\ell$ are unknown complex numbers and $I_{\Delta_\ell}(x)$ is the indicator function of the $\ell$-th triangle, defined as

$$I_{\Delta_\ell}(x) = \begin{cases} 1 & \text{if } x \in \Delta_\ell, \\ 0 & \text{otherwise}, \end{cases}$$

so that $\psi_\ell$ and $\phi_\ell$ are the values of $\psi$ and $\phi$ for all $x$ in $\Delta_\ell$, respectively.

In order to find the densities, the prescriptions (13) are inserted in the system (11). This procedure transforms each integral over the boundary $\Gamma_1$ into a sum of integrals over each triangle $\Delta_\ell$.

The resulting system remains, of course, valid for all $x \in \Gamma_1$, so that is valid in particular for the set of centroids $\{x_\ell\}$ $(\ell = 1, 2, \ldots, N_1)$ of the triangles belonging to $\Gamma_1$. When these discretized equations are evaluated in the set $\{x_\ell\}$, a matrix system of size $2N_1 \times 2N_1$

$$(\boldsymbol{B} + \boldsymbol{D}) \begin{pmatrix} \psi \\ \phi \end{pmatrix} = \begin{pmatrix} \boldsymbol{f} \\ \boldsymbol{g} \end{pmatrix} \tag{14}$$

is obtained. The complex-valued vectors $\psi, \phi$ containing the unknowns and the data vectors $\boldsymbol{f}$ and $\boldsymbol{g}$ are defined as

$$\psi = \begin{pmatrix} \psi_1 \\ \psi_2 \\ \vdots \\ \psi_{N_1} \end{pmatrix}, \quad \phi = \begin{pmatrix} \phi_1 \\ \phi_2 \\ \vdots \\ \phi_{N_1} \end{pmatrix},$$

$$\boldsymbol{f} = -\begin{pmatrix} -\rho_0 \bar{u}^{\mathrm{src}}(x_1) \\ -\rho_0 \bar{u}^{\mathrm{src}}(x_2) \\ \vdots \\ -\rho_0 \bar{u}^{\mathrm{src}}(x_{N_1}) \end{pmatrix}, \quad \boldsymbol{g} = \begin{pmatrix} \partial_n \bar{u}^{\mathrm{src}}(x_1) \\ \partial_n \bar{u}^{\mathrm{src}}(x_2) \\ \vdots \\ \partial_n \bar{u}^{\mathrm{src}}(x_{N_1}) \end{pmatrix}. \tag{15}$$

The complex-valued matrices $\boldsymbol{B}$ and $\boldsymbol{D}$ are defined as 2 block-matrix, each block having size $N_1 \times N_1$

$$\boldsymbol{B} = \begin{bmatrix} (\rho_0 \boldsymbol{K}_0 - \rho_1 \boldsymbol{K}_1) & (\rho_0 \boldsymbol{S}_0 - \rho_1 \boldsymbol{S}_1) \\ -\boldsymbol{M}_{01} & (\boldsymbol{K}_1' - \boldsymbol{K}_0') \end{bmatrix},$$

$$\boldsymbol{D} = \begin{bmatrix} 1/2\alpha_{01} \boldsymbol{I} & \boldsymbol{0} \\ \boldsymbol{0} & \boldsymbol{I} \end{bmatrix}, \tag{16}$$

where $\boldsymbol{I}$ is the identity matrix of dimension $N_1$. The boldface typography used for the operator's matrix representation attempts to capture its discrete nature. For a generic operator $\boldsymbol{U}_q \in \mathbb{C}^{N_1 \times N_1}$ with kernel $\Phi(k_q; x, y)$ the $i, j$ matrix element represents

$$[\boldsymbol{U}_q]_{ij} = \int_{\Delta_j} \Phi(k_q; x_i, y) \, \mathrm{d}S_y.$$

The matrix row-index $i$ is associated with a particular evaluation point $x_i$ while the column index $j$ is associated with the particular element $\Delta_j$. The subindex $q$ identifies the corresponding wavenumber $k_q$. For example,

$$[\boldsymbol{S}_1]_{\ell s} = \int_{\Delta_s} \bar{G}(k_1; x_\ell, y) \, \mathrm{d}S_y$$

implies integration over the $s$-th triangle of $\Gamma_1$ and evaluation on centroid $x_\ell$, all for the wavenumber $k_1$.

Numerical evaluation of the operators can be cumbersome since it involves the resolution of integral singularities. In this case, the computational implementation is strongly based on a previous work that uses the traditional free-space Green function as integral kernel.[30] Thus, the numerical evaluation of the matrix components at Eq. (16) is carried out by taking that previous implementation and changing the Green function. Even though this process is long and implies many calculations, this is straightforward, because as was it previously stated, the kernel is modified by adding a term regular for all $x$, $y$ in the physical domain, meaning that there is no need to develop additional numerical treatments of singularities.

Once the matrix system of Eqs. (14)–(16) is solved and the density vectors $\phi$, $\psi$ are obtained, we are ready to evaluate the field in any point $x$ belonging to the physical domain.

### 2.4. Pressure and TL computation

After having obtained the densities $\psi$, $\phi$, the fields $u_i$ (in water or in the sediment layer) can be calculated by evaluating the corresponding integral representation in Eq. (10) with the piecewise approximation made at Eq. (13). Therefore, using the transformation (2), the discretized version of the pressure field in the water layer is

$$\begin{aligned} p_0(x) \; = \; & -u^{\mathrm{src}\prime}(x) + \sum_{\ell=1}^{N_1} \left( \rho_0 \phi_\ell \int_{\Delta_\ell} \bar{G}(k_0; x, y) \, \mathrm{d}S_y \right. \\ & \left. + \rho_0 \psi_\ell \int_{\Delta_\ell} \partial_{n_y} \bar{G}(k_0; x, y) \, \mathrm{d}S_y \right). \end{aligned} \tag{17}$$

As it is common in acoustic propagation modelling, in the following sections results for acoustic propagation evaluation will be analyzed in the logarithmic scale by using the transmission loss (TL) parameter defined as

$$\mathrm{TL} = -20 \log_{10} \left( \left| \frac{p_0(x)}{p_{\mathrm{ref}}} \right| \right) \quad \text{dB re 1 m}, \tag{18}$$

where the reference pressure $p_{\mathrm{ref}}$ is the pressure evaluated at 1 m from the source.

## 3. Model verifications: Pekeris waveguide

To verify the BEM model, the classical problem of propagation in a Pekeris waveguide is used as a benchmark solution. It consists of a flat homogeneous water layer bounded below by a homogeneous half-space of higher sound speed and above by a pressure-release interface. Such a setup, firstly analyzed within normal mode theory,[31] is a simple but useful model for acoustic propagation in shallow-water ocean environments. This configuration is one of the most employed benchmark solutions because it allows an analytical treatment by using wavenumber integration techniques and it is intrinsically important due to the physical insight that it provides. In the next subsection, an overview of the exact solution and a benchmark case used for verification is presented. Next, comparisons between BEM model and the exact solution are also presented.

### 3.1. Pekeris waveguide solution

The Pekeris waveguide considered as our benchmark setup is shown in Fig. 3. A homogeneous water column of depth $D$, sound speed $c_0$ and density $\rho_0$ overlies a homogeneous fluid half-space of sound speed $c_1$ and density $\rho_1$. A point source located in water at $(r,z)=(0,z_s)$ generates a pressure field

$$p(r,z) = -\rho_0\omega^2 S_\omega \frac{\mathrm{e}^{\mathrm{i}k_0|(r,z)-z_s|}}{4\pi|(r,z)-z_s|},$$

where $S_\omega$ is the source strength. The physical parameters $c$, $\rho$ and location $z_s$ of source and receiver depth $z$ used in this example are taken from an example[25] and explicitly indicated in the figure.

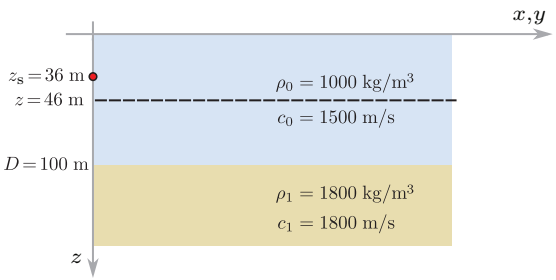



**Fig. 3.** Pekeris waveguide of thickness $D$ = 100 m with pressure-release surface and penetrable bottom. The physical parameters $\rho, c$ in each layer are indicated in the figure.

The pressure $p(r,z)$ in the Pekeris waveguide is then given by

$$p(r,z) = \begin{cases} \rho_0\omega^2\psi_0(r,z), & 0 \le z \le D, \\ \rho_1\omega^2\psi_1(r,z), & z \ge D, \end{cases}$$

where $\psi_i$ ($i=0,1$ corresponding to the water and sediments layers, respectively) are the displacement potentials, which can be expressed as Hankel transforms

$$\psi_i(r,z) = \int_0^\infty \Psi_i(k_r,z) J_0(k_r r) k_r \,\mathrm{d}k_r,$$

with $J_0$ the cylindrical Bessel function of first kind and $\Psi_i(k_r,z)$ the solution of the depth-dependent wave equation

$$\left(\frac{\mathrm{d}^2}{\mathrm{d}z^2} + k_{z,i}^2\right)\Psi_i(k_r,z) = \frac{S_\omega}{2\pi}\delta(z-z_s),$$

where $k_{z,i}^2 = k_i^2 - k_r^2$ is the vertical wavenumber in the $i$-medium. Attenuation in the sediment layer is taken into account trough a complex wavenumber $k_1(1+\mathrm{i}\eta\alpha)$, where the coefficient $\alpha > 0$ quantifies its strength and $\eta = 1/(40\pi\log_{10}e)$ is a numeric constant turning dimensionless the imaginary part. Usually, attenuation $\alpha$ is given in dB/wavelength. Further details and physical analysis of this solution can be founded in Refs. [25,32].

### 3.2. BEM model applied to the Pekeris waveguide

The BEM model was compared to the Pekeris benchmark solution previously presented at frequency $f = 5$ Hz by evaluating transmission loss (TL) (a) along a 2500 m path at $z = 46$ m depth (inside the water layer, see Fig. 3) and (b) in a rectangle 2500 m width and 150 m depth which encompass both water and sediment field evaluations. Two cases are considered: without attenuation and with an attenuation $\alpha = 5$ dB/$\lambda$ (from the applications standpoint is a somewhat big value, its inclusion being justified only to test the model in a broad spectrum of its parameters). All the simulations were conducted over a circular mesh of radius $R = 2500$ m and $N = 49009$ triangles which represents the boundless interface water-sediments.

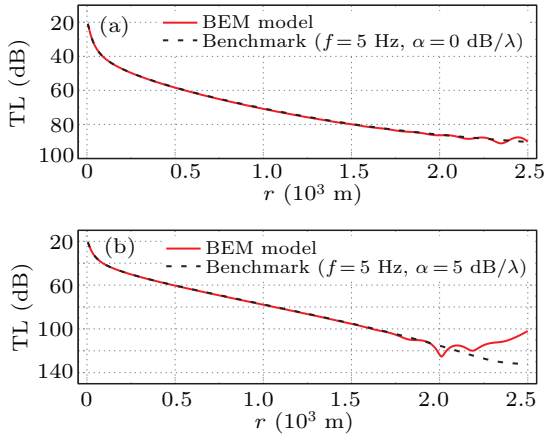



**Fig. 4.** Transmission loss (TL) vs. range computed by the BEM model (full lines) and by the wavenumber benchmark solution (dashed lines) for a Pekeris waveguide with thickness of 100 m (physical, source and evaluation parameters given in Fig. 3) along a 2.5 km path with depth $z = 46$ m. Source frequency $f = 5$ Hz. (a) Without attenuation ($\alpha = 0$ dB/$\lambda$). (b) With attenuation given by $\alpha = 5$ dB/$\lambda$.

Since our BEM formulation assumes constant field on each triangle, the number $N$ of elements of the mesh must be chosen to ensure that the acoustic wavelength would be several times greater than the distance between vertices (usually five or six times greater) according to the usual practice in scattering applications.[33] In the circular mesh used for this verifi-

cation test, the previous requirement is fulfilled by the 96% of the triangle' sides.

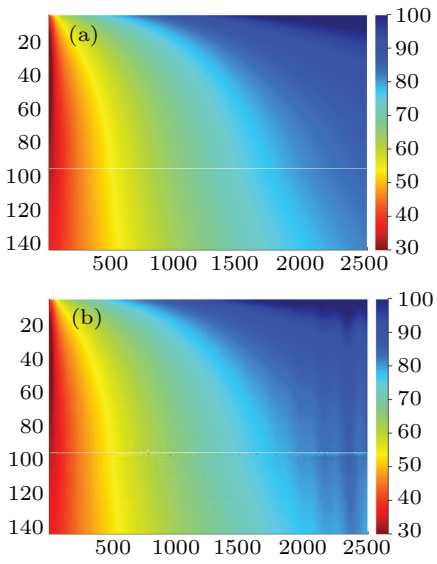



**Fig. 5.** Transmission loss (TL) vs. range and depth, evaluated for the rectangle $0 \le r \le 2500$ m and $0 \le z \le 150$ m (without attenuation). Benchmark solution (a) and BEM solution (b) for $f = 5$ Hz. The interface water-sediments is indicated by a white line.

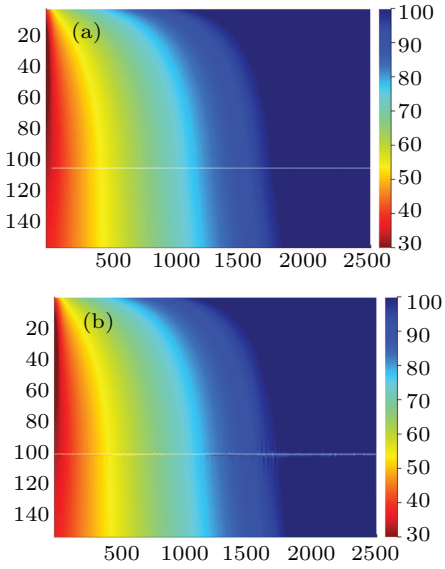



**Fig. 6.** Transmission loss (TL) vs. range and depth evaluated for the rectangle $0 \le r \le 2500$ m and $0 \le z \le 150$ m (with attenuation given by $\alpha = 5$ dB/$\lambda$). Benchmark solution (a) and BEM solution (b) for $f = 5$ Hz. The interface water-sediments is indicated by a white line.

The results of the comparison are shown in Fig. 4, where panel (a) shows the case without attenuation ($\alpha = 0$) and panel (b) the case with the strong attenuation $\alpha = 5$ dB/$\lambda$. The evaluation coordinate $r$ reaches the end of the mesh so that errors are expected there. They are evident in the case $\alpha \neq 0$ but slightly noticeable in the $\alpha = 0$ dB/$\lambda$ case. The former assumption about the pseudo-local character of the fields, i.e., the fact that the boundary values of the field at very long distances are not required to determine the field in a restricted domain, appears to be a valid one. Of course, in cases where a benchmark solution is not available, which portions of the domain need to be meshed should be the object of analysis.

Figures 5 and 6 show the transmission losses for a rectangle, which encompasses water and sediments in the cases of $\alpha = 0$ and $\alpha = 5$ dB/$\lambda$ of attenuation, respectively. A solid white line indicates the interface between both media. Panels (a) show the benchmark solution whereas panels (b) are the results provided by the BEM model. In all the figures, colorbars are saturated in the interval [30,100] dB for clarity purposes in the comparison. The evaluations are visually in good agreement although there are some numerical artifacts near the interface line, which are a consequence of the evaluation point closeness in regard the triangle' sides in the interface mesh. This perturbations can be avoided by considering a finer mesh.

### 3.3. Effect of the finiteness of the mesh

The theoretical propagation problem involves, as previously mentioned, unbounded layers. The formulation based on the half-space Green function considers the pressure-release water surface in an exact form, including also its intrinsic nofiniteness, but conversely the water-sediments interface must be discretized – taking into account the relationship between wavelength and segment length – which arises a natural question: how far should this discretization go?

The previous verifications *a priori* assumed that the region surrounding the source will be mandatory for an accurate representation of the field in the modelling, therefore the source was centered regarding the disk constituting the mesh of the bottom surface. To quantify the suitability of this centered-source assumption, we evaluate the TL corresponding to the Pekeris waveguide (at $f = 5$ Hz and $\alpha = 0$ dB/$\lambda$) with the circular mesh of 2.5 km radius and $N = 49009$ triangles but shifting radially the source location in 625 m, 1250 m and 2500 m. This provides four configurations labelled as $A$, $B$, $C$ and $D$ being the first of them the original configuration (null shift).

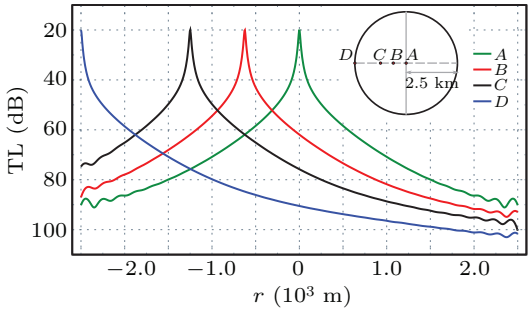



**Fig. 7.** Transmission loss (TL) vs. range computed by the BEM model for the Pekeris waveguide along a 5000 m radial path coincident with a radius of the circular mesh of $N = 49009$ triangles. The source were located at $z_s = 36$ m but shifted radially in $r$ according to the scheme shown in the insert. The configurations $A$, $B$, $C$ and $D$ have the source at 0 m, −625 m, −1250 m and −2500 m in the coordinatization used.

The resulting TL are shown in Fig. 7, where the inset in the upper right corner identifies the source location in each case. The source shift is indicated by a negative $r$-coordinate.

The finite size of the mesh is clearly noticeable at each side of the curves (except in the $D$ case) and the source location is evidenced by the sharp peak corresponding to minimum TL, which is obtained at the minimum distance $(z - z_s)$ between source and evaluation point.

To quantify the error in each TL computation, the resulting curves $B$, $C$, and $D$ are shifted to match with $A$. Then they are comparable point to point alongside a line of 2500 m, which is the minimum length common to all of them. Defining a relative error in the logarithmic scale according to

$$\text{Rel Err} = \frac{|\text{TL} - \text{TL}_\text{b}|}{|\text{TL}_\text{b}|}, \tag{19}$$

where $\text{TL}_\text{b}$ is the Pekeris wavenumber integration prediction (the benchmark), errors associated to the different TL obtained in the four cases can be quantified. Results are shown in Fig. 8. An inset in the left side shows a scheme for source location in each configuration $A$, $B$, $C$ and $D$ as well as the 2.5 km line segment (dashed lines) where the TL are being calculated in each case (for clarity purposes – avoiding the overlapping – in this scheme the lines are shifted a little amount in the vertical direction).

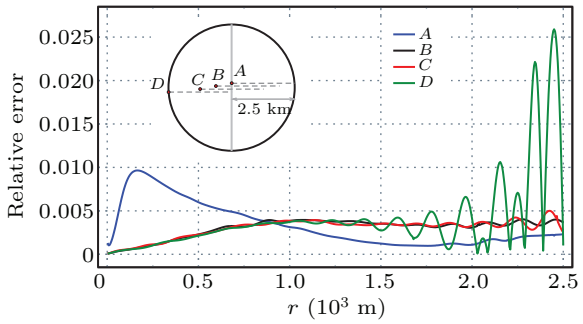



**Fig. 8.** Relative error, according to definition (19), for the TL vs. range $r$ (distance to the source) of shifted source configurations $A, B, C$ and $D$. In each case the first 2500 m from the source to the right were compared point to point with the benchmark solution. The inset in the upper left corner shows the evaluation segment compared for each case.

The $A$ configuration, i.e., the source "centered" at the mesh, shows the expected error of mesh-finiteness already observed, clearly amplified towards the end of the line (beyond $r = 2500$ m there is no world!). Configurations $B$ and $C$, sources shifted in 625 m and 1250 m, result in a better error behaviour, because for neither one a relative error of 0.005 is surpassed. Remarkably, TL evaluation for the immediate region surrounding the source is not perturbed in these shifted cases. The extreme case of a source located in the border of the domain, configuration $D$, exhibits a maximum error in the first 250 m but a decreasing one afterwards.

These numerical experiments reveal that a compromise solution between accuracy and mesh size for TL calculation, along lines at least, can be attained considering a centered line of evaluation more than a centered source. The associated question arising next is, assuming that a centered configuration as $C$ satisfies a desired error, how to surround that segment with a mesh big enough to provide an "accurate" TL evaluation but simultaneously with little overhead due to calculation from far regions with negligible contribution. To explore this question we considered two alternative meshes built from the original circular disk: two ellipses of 2500 m major axis and minor axis in the relation 1:2 and 1:3, which results in 1250 m and 833.33 m, respectively.

The two elliptical meshes were built assuring a triangle density similar to the one used in the circular mesh. Therefore, the ellipses 1:2 and 1:3 have $N = 24628$ and $N = 16285$ triangles, respectively. The relation between areas with respect to the 2500 m radius circular disk are 1/2 and 1/3 whereas the relation between the number of triangles are 0.502 and 0.332. Therefore, the triangle density (defined as the number of mesh triangles per area unit) is similar for all the three meshes.

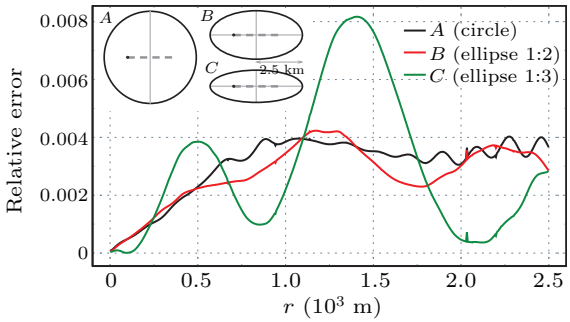



**Fig. 9.** Relative error for TL vs. range evaluated for a 2500 m segment, which is indicated by dashed lines in the scheme of the inset, for the 2500 m radius circular mesh and two elliptical meshes with major semiaxes of 2500 m and minor semiaxes in ratios 1:2 and 1:3.

In Fig. 9 the relative error for TL calculation along a 2500 m line for the three meshes considered is shown. The inset at the upper left corner of the figure details the evaluation segment for the circular and the elliptical meshes. Surprisingly, the decrease in the extension of the mesh has no appreciable effect in the TL since the relative error is similar. The 1:3 ellipse displays an oscillatory behaviour, which emerges as an artifact introduced by the artificial elliptic boundary delimiting the end of the computational domain. Elliptical meshes with an increased number of triangles and other aspect-ratio as 1:4, display similar behaviors in $r$. Nevertheless, for the 1:3 ellipse, these relative errors do not exceed 0.64 dB in absolute terms, a value which is acceptable in practical applications of acoustical propagation in the ocean. In addition, the nominal number of triangles in this case is significantly lower than the circle, which has direct consequences in reducing the computing time.

## 4. BEM model in a shallow waters range dependent environment

To evaluate the model in a range dependent environment, we have built a synthetic scenario provided with a non-trivial

bathymetry consisting of a plane bottom of $D = 500$ m depth with a conical mountain with a height of 300 m inside. Similar scenarios were used, for example, in Refs. [5,34]. Transmission losses will be evaluated over a $r$, $z$ plane of $2500\times1000$ m, which cuts in half the mountain. A point source of unitary amplitude and frequency $f = 5$ Hz is located at $r = 0$ and $z_s = 250$ m. A mesh of circular shape with radius $R = 2500$ m containing the mountain surface will be used. Figure 10 shows a 2D sketch of the evaluation plane with the physical parameters indicated over it (a) and a 3D view encompassing both the plane and the water-sediments interface mesh (b).

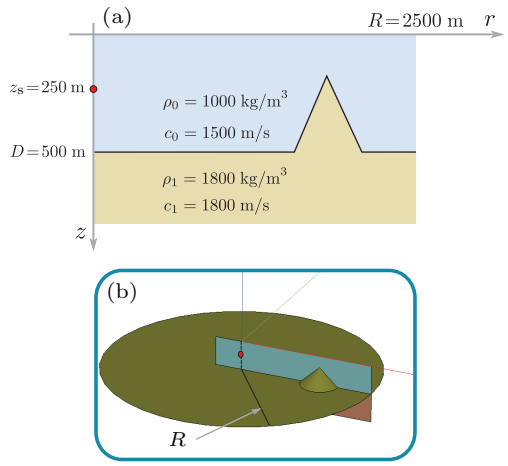



**Fig. 10.** Scheme for a range dependent waveguide environment; a plane bottom with a depth of 500 m provided with a 300 m height conical mountain. TL will be evaluated over a plane of $2500 \times 1000$ m in $r$, $z$ which is shown with the propagation parameters overimposed (a) and in a 3D panoramic view (b).

The circular mesh has $N = 50000$ triangles. The given frequency involves acoustics wavelengths of $\lambda_0 = 300$ m and $\lambda_1 = 360$ m for the water and sediments, respectively. Considering a maximum segment length of $\lambda/5$, and taking into account the lower wavelength, it leads to a triangle' sides $\ell < 60$ m. This condition was fulfilled for the 95% of the triangles of the mesh.

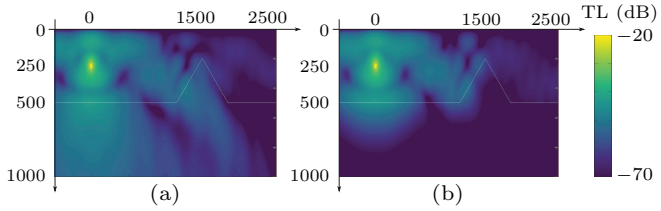



**Fig. 11.** Transmission loss (TL) evaluated over the $(r,z)$-plane previously shown in the Fig. 10. The white line indicates the water-sediments interface. Panel (a) considers attenuation $\alpha = 0$ whereas (b) $\alpha = 20$ dB/$\lambda$. The color bar on the right is saturated for a better contrast; all TL values greater than $-20$ dB appears as $-20$ dB.

For TL evaluation two attenuation coefficients were used: $\alpha = 0$ (no attenuation) and $\alpha = 20$ dB/$\lambda$. The latter value big enough only aimed to show a remarkably different graphical result. In Fig. 11, results for TL in the $rz$-plane are shown: the no attenuation case (a) and the $\alpha = 20$ dB/$\lambda$ one (b). The color bar values were saturated for a better contrast. The water-sediments interface is indicated by a white line showing that the TL changes continuously when the interface is crossed. The region surrounding the source shows brighter indicating low TL values as expected.

The intense attenuation due to the selected $\alpha$-value accounts for the fast vanishing of the pressure field and consequent increase of the transmission losses. Moreover, it is noticeable that the conical mountain presence does not preclude appreciably pressure fields behind it, which are an effect of the relative low frequency and diffraction effects due to the boundaries.

## 5. Conclusions

An indirect BEM approach was proposed and numerically implemented to solve an underwater acoustic propagation problem that provides an stable and clean formulation as a consequence of avoiding the intrinsic instabilities of the direct methods and the automatic fulfilling of the radiation condition for the fields at infinity. There was no need of artificial boundaries and layers, required in other methods to avoid emergence of spurious numerical artifacts. Numerical experiments have shown that discretization of the entire domain boundary is not necessary to achieve an acceptable prediction but this "local approach" to the problem still can be computationally demanding at the frequency ranges of interest for some applications. The formulation based on a half-space Green function has required some tweaking of the integral operators for enabling to consider an infinite pressure release surface (Dirichlet condition). This modification avoids the need of building a mesh for the seawater-atmosphere interface, which would have required to build and handle a matrix system two-times bigger. An infinite acoustic hard surface (Neumann condition) suitable for modelling propagation over a rigid bottom can be worked out in the same fashion with minor modifications.

For an admissible accuracy in the TL evaluation, a mesh considering a limited region near the source is enough. Even for moderated frequencies this implies very large matrix systems, and thus, there is a clear need of iterative methods for the system solving stage and accelerated integral evaluations, two key components to circumvent the explicit matrix construction and to allow a fast evaluation of the matrix elements, respectively.

There are plenty of works where iterative methods and accelerated integrations are employed (see Refs. [35,36] and references therein). The former obviously is not restricted to the narrow context of boundary integration methods since the tackling of large matrix systems is a common feature in the realm of numerical methods when physical systems with many degrees of freedom are under analysis. Computational

implementations are readily available in all the popular programming languages. The accelerated evaluation of integrals, by contrast, is a more specific topic and is closely related to the fast multipole method (FMM),[37–39] which is an algorithm aimed to speed up the calculations in many body systems.

To extend and improve the numerical implementation of the BEM formulation presented in this work, the following steps would require: (a) incorporate an iterative solver to the matrix system solving stage of the propagation problem; and (b) design and build an acceleration algorithm for the numerical evaluation of the integrals which can handle its singular behaviour. Surely, this road map will benefit from all the previous work carried out in other branches of physical sciences.

## Appendix A: Boundary integral equation from boundary conditions at $\Gamma_1$

Evaluation of an integral operator $U[\varphi]$ at a boundary point $x \in \Gamma_1$ approached from the region $R_0$ is calculated as the limit

$$U[\varphi](x) = \lim_{h\to 0} U[\varphi](x + h\hat{n}),$$

where $x$ is reached along the normal direction given by $\hat{n}$ (the normal at $x$) from the point $x_0 \in R_0$ (see Fig. A1). The operator evaluation at $x$ but approached from the region $R_1$ proceed along the opposite direction (i.e., along $-\hat{n}$) from the point $x_1 \in R_1$, i.e.,

$$U[\varphi](x) = \lim_{h\to 0} U[\varphi](x - h\hat{n}),$$

where $h > 0$ in both cases.

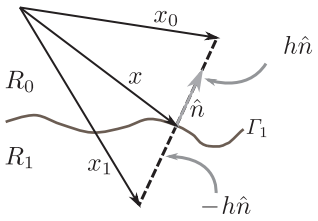



**Fig. A1.** Sketch for normal derivative evaluation.

By inserting the prescriptions (10) in Eqs. (4) and defining $x^+ = x + h\hat{n}$ and $x^- = x - h\hat{n}$ the boundary conditions can be considered as $h \to 0$ limits,

$$\begin{aligned}
&\lim_{h\to 0} \rho_0 (S_0[\phi](x^+) + K_0[\psi](x^+) + \bar{u}^{\mathrm{src}}(x^+)) \\
&= \lim_{h\to 0} \rho_1 (S_1[\phi](x^-) + K_1[\psi](x^-)), \\
&\lim_{h\to 0} K_0'[\phi](x^+) + T_0[\psi](x^+) + \partial_n \bar{u}^{\mathrm{src}}(x^+) \\
&= \lim_{h\to 0} K_1'[\phi](x^-) + T_1[\psi](x^-),
\end{aligned}$$

where the evaluation point $x^+$ tends to $\Gamma_1$ from $R_0$ whereas point $x^-$ tends from $R_1$. Evaluating the $h \to 0$ limit and considering the jump (jump and continuity conditions, see theorem 3.1 of Ref. [24]) for $K_i$ and $S_i$, we obtain

$$\begin{aligned}
&\rho_0 S_0[\phi](x) - \rho_1 S_1[\phi](x) + \rho_0 K_0[\psi](x) \\
&\quad - \rho_1 K_1[\psi](x) + \alpha_{01} I[\psi](x) = -\rho_0 \bar{u}^{\mathrm{src}}(x), \\
&K_0'[\phi](x) - K_1'[\phi](x) - I[\phi](x) \\
&\quad + T_0[\psi](x) - T_1[\psi](x) = -\partial_n \bar{u}^{\mathrm{src}}(x),
\end{aligned}$$

where $\alpha_{01} = (\rho_0 + \rho_1)/2$ and $I$ is the identity operator. By using the definition of the Müller operator, Eq. (12), and a more compact notation, the boundary conditions result in

$$\begin{aligned}
&(\rho_0 S_0 - \rho_1 S_1)[\phi](x) \\
&+ (\rho_0 K_0 - \rho_1 K_1 + \alpha_{01} I)[\psi](x) = -\rho_0 \bar{u}^{\mathrm{src}}(x), \\
&(K_0' - K_1' - I)[\phi](x) + M_{01}[\psi](x) = -\partial_n \bar{u}^{\mathrm{src}}(x).
\end{aligned}$$

By multiplying the last equation by $-1$, an usual convention, it results in the boundary integral system of Eq. (11).

## Appendix B: Operator's expressions for $\bar{G}$

The cartesian coordinate system associated with the problem is shown in Fig. B1.

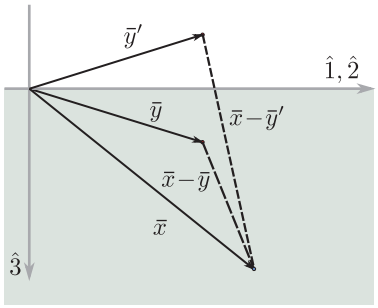



**Fig. B1.** Coordinate system used for the graphical representation of vectors and distances involved in the half-space Green function operator's expressions.

Throughout this appendix the vector property will be explicitly emphasized by a line over the corresponding letter for clarity reasons and to avoid confusions. With this convention the points under consideration are $\bar{x} = (x_1, x_2, x_3)$, $\bar{y} = (y_1, y_2, y_3)$ and $\bar{y}' = (y_1, y_2, -y_3)$, being useful to define

$$r = |\bar{x} - \bar{y}|, \quad r' = |\bar{x} - \bar{y}'|$$

and unitary vectors

$$\hat{r} = \frac{\bar{x} - \bar{y}}{r} = \frac{\bar{r}}{r}, \quad \hat{r}' = \frac{\bar{x} - \bar{y}'}{r'} = \frac{\bar{r}'}{r'}.$$

The half-space Green function in the wavenumber $k$ is

$$\bar{G}(k, \bar{x}, \bar{y}) = \frac{e^{ik|\bar{x}-\bar{y}|}}{4\pi|\bar{x}-\bar{y}|} - \frac{e^{ik|\bar{x}-\bar{y}'|}}{4\pi|\bar{x}-\bar{y}'|} = \frac{e^{ikr}}{4\pi r} - \frac{e^{ikr'}}{4\pi r'}. \quad \text{(B1)}$$

Given that the Green function is a two-point function, it is relevant to indicate respect to what point the gradient is considered. It will be noted with a subscript in the nabla symbol: $\nabla_x$ or $\nabla_y$. Since the dependence of the coordinates in $\bar{G}$ is mediated by $r$ and $r'$, it is convenient to use the chain rule

$\nabla f(r) \equiv \partial_r f \nabla r$ and $\nabla f(r') \equiv \partial_{r'} f \nabla r'$ in the gradient calculation. By using this idea and the relations

$$\nabla_x r = \frac{\bar{r}}{r}, \quad \nabla_y r = -\frac{\bar{r}}{r}, \quad \nabla_x r' = \frac{\breve{r}'}{r'}, \quad \nabla_y r' = -\frac{1}{r'}\breve{r}',$$

where $\breve{r}'$ is a vector resulting from multiplying $\bar{r}'$ by a diagonal matrix which has its third coordinate negative, i.e.,

$$\breve{r}' = \begin{pmatrix} 1 & 0 & 0 \\ 0 & 1 & 0 \\ 0 & 0 & -1 \end{pmatrix} \bar{r}',$$

the following useful results are obtained:

$$\nabla_x \left( \frac{\mathrm{e}^{\mathrm{i}kr}}{4\pi r} \right) = \frac{\mathrm{e}^{\mathrm{i}kr}}{4\pi r^3} (\mathrm{i}kr - 1)\, \bar{r},$$

$$\nabla_x \left( \frac{\mathrm{e}^{\mathrm{i}kr'}}{4\pi r'} \right) = \frac{\mathrm{e}^{\mathrm{i}kr}}{4\pi r'^3} (\mathrm{i}kr' - 1)\, \bar{r}',$$

$$\nabla_y \left( \frac{\mathrm{e}^{\mathrm{i}kr}}{4\pi r} \right) = -\frac{\mathrm{e}^{\mathrm{i}kr}}{4\pi r^3} (\mathrm{i}kr - 1)\, \bar{r},$$

$$\nabla_y \left( \frac{\mathrm{e}^{\mathrm{i}kr'}}{4\pi r'} \right) = -\frac{\mathrm{e}^{\mathrm{i}kr}}{4\pi r'^3} (\mathrm{i}kr' - 1)\, \breve{r}'.$$

With these ingredients, the kernels of the four operators are as follows. For $S[\varphi](x)$

$$\bar{G}(x,y) = \frac{1}{4\pi} \left[ \frac{\mathrm{i}kr}{r} - \frac{\mathrm{i}kr'}{r'} \right].$$

For $K[\varphi](x)$

$$\partial_{n_y} \bar{G}(x,y) = \frac{1}{4\pi} \left[ \frac{\mathrm{i}kr}{r^2} (\mathrm{i}kr - 1)(-\hat{r} \cdot \hat{n}_y) - \frac{\mathrm{i}kr'}{r'^2} (\mathrm{i}kr' - 1) \left( -\frac{\breve{r}'}{r'} \cdot \hat{n}_y \right) \right].$$

For $K'[\varphi](x)$

$$\partial_{n_x} \bar{G} \mathrm{d}S_y = \frac{1}{4\pi} \left[ \frac{\mathrm{i}kr}{r^2} (\mathrm{i}kr - 1)(\hat{r} \cdot \hat{n}_x) - \frac{\mathrm{i}kr'}{r'^2} (\mathrm{i}kr' - 1) \left( \hat{r}' \cdot \hat{n}_x \right) \right].$$

For $T[\varphi](x)$

$$\begin{aligned} &\partial_{n_x} \partial_{n_y} \bar{G}_k(x,y) \\ &= \frac{\mathrm{e}^{\mathrm{i}kr}}{4\pi r^3} \left\{ [3(\mathrm{i}kr - 1) + k^2 r^2](\hat{r} \cdot \hat{n}_x)(\hat{r} \cdot \hat{n}_y) - (\mathrm{i}kr - 1)\hat{n}_x \cdot \hat{n}_y \right\} \\ &+ \frac{\mathrm{e}^{\mathrm{i}kr'}}{4\pi r'^3} \left\{ [3(\mathrm{i}kr' - 1) + k^2 r'^2](\hat{r} \cdot \hat{n}_x) \left( \frac{\breve{r}'}{r'} \cdot \hat{n}_y \right) \right. \\ &\left. - (\mathrm{i}kr' - 1)\partial_{n_x} (\breve{r}' \cdot \hat{n}_y) \right\}, \end{aligned}$$

where the last factor in the second term of the $T$ operator is

$$\partial_{n_x} (\breve{r}' \cdot \hat{n}_y) = \hat{r}' \cdot \hat{n}_x \left( \frac{\breve{r}'}{r'} \right) \cdot \hat{n}_y + \hat{n}_x \cdot \begin{pmatrix} 1 & 0 & 0 \\ 0 & 1 & 0 \\ 0 & 0 & -1 \end{pmatrix} \hat{n}_y - \hat{n}_x \cdot \left( \frac{\breve{r}'}{r'} \right) \hat{r}' \cdot \hat{n}_y.$$

## References


[1] Buckingham M J 1992 *Journal d'acoustique (Les Ulis)* **5** pp. 223–287

[2] Tolstoy A 1996 *J. Comp. Acous.* **04** 243

[3] Sturm F and Korakas A 2013 *J. Acoust. Soc. Am.* **133** 108

[4] Oliveira T C, Lin Y T and Porter M B 2021 *Front. Marine Sci.*, pp. 1464

[5] Lin Y T, Duda T F and Newhall A E 2013 *J. Comp. Acous.* **21** 1250018

[6] Heaney K D and Campbell R L 2016 *J. Acoust. Soc. Am.* **139** 918

[7] Lin Y T, Newhall A E, Miller J H, Potty G R and Vigness-Raposa K J 2019 *J. Acoust. Soc. America* **145** 335

[8] Taroudakis M I, Athanassoulis G A and Ioannidis J P 1990 *J. Acoust. Soc. Am.* **88** 1515

[9] Porter M B 1992 *Technical report, Naval Research Lab Washington DC*

[10] DeCourcy B J and Duda T F 2020 *J. Acoust. Soc. Am.* **148** 51

[11] Tu H, Wang Y, Lan Q, Liu W, Xiao W and Ma S 2021 *J. Sound Vibrat.* **511** 116364

[12] de Moraes Calazan R and Rodríguez O C 2018 *J. Acoust. Soc. Am.* **143** 2059

[13] Porter M B 2019 *J. Acoust. Soc. Am.* **146** 2016

[14] Zhu Z J, Ma S Q, Zhu X Q, Lan Q, Piao S C and Cheng Y S 2022 *Chin. Phys. B* **31** ac7ccc

[15] Boyles, C A 1984 *Acoustic Waveguides: Applications to Oceanic Science* (John Wiley and Sons Inc)

[16] Li, C, Campbell B K, Liu Y and Yue D K 2019 *J. Comput. Phys.* **392** pp. 694–712

[17] Prario I, Cinquini M, Marques Rojo R, Gonzalez J D, Lavia E, Bos P and Blanc S 2022 *Pure and Applied Geophysics* **179** 1

[18] Wu L L and Peng Z H 2015 *Chin. Phys. Lett.* **32** 094302

[19] Dawson T W and Fawcett J A 1990 *J. Acoust. Soc. Am.* **87** 1110

[20] Santiago, J A F and Wrobel L C 2000 *Comput. Model. Eng. Sci.* **1** pp. 73–80

[21] Santiago J A F and Wrobel L C 2004 *Eng. Anal. Bound. Elem.* **28** 1375

[22] Seybert A F and Soenarko B 1998 *J. Vib. Acoustics* **110** 112

[23] Kress R and Roach, G 1978 *J. Mathemat. Phys.* **19** pp. 1433–1437

[24] Colton D and Kress R 1998 *Inverse acoustic and electromagnetic scattering theory*, volume 93 (Springer-Verlag Berlin)

[25] Jensen F B, Kuperman W A, Porter M B, Schmidt, H and Tolstoy A 1994 *Computational Ocean Acoustics* (American Institute of Physics)

[26] Smith K B 2001 *J. Comput. Acoust.* **9** 243

[27] Liu R Y and Li Z L 2019 *Chin. Phys. B* **28** 014302

[28] Tappert F and Nghiem-Phu L 1985 *J. Acoust. Soc. Am.* **77** S101

[29] Kress R 2001 *Scattering, Two-Volume Set: Scattering and Inverse Scattering in Pure and Applied Science*, (Elsevier) pp. 37–51

[30] Gonzalez J D, Lavia E F, Blanc S, Maas M and Madirolas A 2020 *J. Sound Vibrat.*, **486** 115609

[31] Pekeris C L 1948 *Geol. Soc. Am, Memoir* **27**

[32] Luo W Y, Yu X L, Yang X F and Zhang R H 2016 *Chin. Phys. B* **25** 044302

[33] Foote K G 1980 *J. Acoust. Soc. Am.* **67** 2084

[34] Mo Y X, Zhang C J, Lu L C and Guo S M 2022 *Chin. Phys. B* **28** 084301

[35] Yan Z Y and Gao X W 2013 *Engineer. Analys. Bound. Elements* **37** 409

[36] Li C and Lian J 2020 *Appl. Sci.* **10** 2393

[37] Greengard, Leslie and Vladimir Rokhlin 1987 *J. Comput. Phys.* **73** 325

[38] Li S D, Huang Q B and Li T Y 2012 *Acta Phys. Sin.* **61** 064301 (in Chinese)

[39] Wu H Y and Jiang W 2012 *Acta Phys. Sin.* **61** 054301 (in Chinese)